Title

Ferroelectricity in a semiconducting all-inorganic halide perovskite

Permalink

https://escholarship.org/uc/item/4vj925mz

Journal

Science Advances, 8(6)

ISSN

2375-2548

Authors

Zhang, Ye
Parsonnet, Eric
Fernandez, Abel
et al.

Publication Date

2022-02-11

DOI

10.1126/sciadv.abj5881

Peer reviewed

Ferroelectricity in a semiconducting all-inorganic halide perovskite

Ye Zhang[1], Eric Parsonnet[2], Abel Fernandez[3], Sinéad M. Griffin[4,5], Huaixun Huyan[6], Chung-Kuan Lin[1,4], Teng Lei[1], Jianbo Jin[1], Edward S. Barnard[5], Archana Raja[5], Piush Behera[3,4], Xiaoqing Pan[6,7,8], Ramamoorthy Ramesh[2,3,4,*], Peidong Yang[1,3,4,9,*]

[1]Department of Chemistry, University of California, Berkeley, CA 94720, USA.

[2]Department of Physics, University of California, Berkeley, CA 94720, USA.

[3]Department of Materials Science and Engineering, University of California, Berkeley, CA 94720, USA.

[4]Materials Science Division, Lawrence Berkeley National Laboratory, Berkeley, California 94720, USA.

[5]Molecular Foundry, Lawrence Berkeley National Laboratory, Berkeley, California 94720, USA.

[6]Department of Materials Science and Engineering, University of California, Irvine, CA 92697, USA.

[7]Department of Physics and Astronomy, University of California, Irvine, CA 92697, USA.

[8]Irvine Materials Research Institute, University of California, Irvine, CA 92697, USA.

[9]Kavli Energy NanoScience Institute, Berkeley, CA 94720, USA.

*Corresponding authors. E-mails: p_yang@berkeley.edu (P.Y.); rramesh@berkeley.edu (R.R.).

One-sentence summary: An inorganic germanium halide perovskite as a new ferroelectric semiconductor features visible light responses and switchable polarizations.

ABSTRACT

Ferroelectric semiconductors are rare materials possessing both spontaneous polarizations and visible light absorptions that are promising for designing functional photoferroelectrics, such as optical switches and ferroelectric photovoltaics. The emerging halide perovskites with remarkable semiconducting properties also have the potential of being ferroelectric, yet the evidence of robust ferroelectricity in the typical three-dimensional (ABX_3 form) hybrid halide perovskites has been elusive. Here we report the first investigation of ferroelectricity in all-inorganic halide perovskites, $CsGeX_3$ (X=Cl, Br, I), with bandgaps of 1.6-3.3 eV. Their ferroelectricity originates from the lone pair stereochemical activity in Ge (II) that promotes the ion displacement. This gives rise to their spontaneous polarizations of ~10-20 $\mu C/cm^2$, evidenced by both *ab initio* calculations and key experiments including atomic-level ionic displacement vector mapping and ferroelectric hysteresis loop measurement. Furthermore, characteristic ferroelectric domain patterns on the well-defined $CsGeBr_3$ nanoplates are imaged with both piezo-response force microscopy and nonlinear optical microscopic method.

INTRODUCTION

Ferroelectrics are characterized by a switchable spontaneous polarization that results from long-range ordered electric dipoles (*1*). The switching of polarization under applied electrical field, as well as the control of polarization responses with temperature or strains, make ferroelectric materials desirable for various technologies including switching devices, sensors and non-volatile memories (*2*, *3*). Coupling ferroelectricity with photo excitation in semiconductors could further enhance the material functionality, whereby light can take the role of an additional control knob for inducing new physical phenomena and tuning properties beyond the conventional ferroelectric behaviors (*4–7*). Particular examples include the optically controlled polarizations (*8*) for optical switches and polarization-induced charge separation being called ferroelectric photovoltaic effect (*4–6*, *9*, *10*). However, the design of effective optical switches or ferroelectric photovoltaics under solar illumination critically depends on materials with both substantial polarizations and efficient visible light absorptions, that is, ferroelectric semiconductors.

Since the prototypical ferroelectrics such as perovskite oxides (ABO$_3$) generally have wide bandgaps (3–5 eV) with very few exceptions, *i.e.* BiFeO$_3$ (2.7 eV), the search and design of ferroelectrics with suitable bandgaps in the visible regions has attracted much attention. Among these efforts, elemental doping in the oxide perovskites has proven effective in achieving reduced bandgaps, exemplified by Ni-doped KNbO$_3$ and PbTiO$_3$ (*10*, *11*). The identification of ferroelectricity in other semiconducting non-perovskite systems such as SbSI (*12*) and GeTe (*13*) have also been reported, though an unstable ferroelectricity in these materials has sparked debates (*1*). Low carrier mobilities or weak light absorptions also limit the application of all these material platforms.

Halide perovskites (ABX$_3$, X are halides) are structurally analogous to the oxide perovskites but are readily a new class of semiconductors by themselves (bandgaps of 1–3 eV), different from their wide-bandgap insulating oxide counterparts. Much research has focused on the unprecedented performance of halide perovskites as photoactive materials for optoelectronics due to their strong light absorption, tunable photoresponse, efficient carrier transport properties as well as ease of processing (*14–17*). It is thus intriguing to explore the potential ferroelectricity in halide perovskites, where the coupling among these behaviors may result in the emergence of new ferroelectric semiconductors. Although ferroelectric responses have been reported in some organic-inorganic halide perovskites (*18*, *19*), the nature of the polar order in some of the hybrid materials (*e.g.* CH$_3$NH$_3$PbI$_3$) still remains unclear as the dynamic organic species with chemical and mechanical inhomogeneities can obscure the origin of the polarity and ferroelectric domain-like features (*20*, *21*). On the other hand, it is highly desirable to exclude the volatile organic components that are thermally unstable and develop all-inorganic candidates for practical device fabrications.

CsGeX$_3$ (X=Cl, Br, I) is the only class of inorganic halide perovskites with a non-centrosymmetric crystal structure (*22–24*) that could lead to potential ferroelectric properties. Here, we present the experimental discovery of ferroelectricity in semiconducting CsGeX$_3$. We attained the synthetic control for producing single-crystalline CsGeBr$_3$ nanowires and nanoplates by facile chemical vapor transport methods. The CsGeBr$_3$ nanostructures have a bandgap of 2.38 eV, exhibiting strong visible light absorption and photoresponses. Atomic displacement vector mapping and macroscopic polarization hysteresis loop measurement (on both CsGeBr$_3$ nanowire and CsGeI$_3$ thin film) established the existence of ferroelectricity, with the spontaneous polarization of ~10-20 μC/cm^2 that matches with *ab initio* calculations. Moreover, the well-defined CsGeBr$_3$

nanoplates are especially suitable for imaging the self-organized polar domains using piezo-response force microscopy and polarization-resolved second harmonic generation microscopy. We anticipate that this study will open a pathway for further exploration into this class of semiconducting ferroelectric materials and trigger new possibilities in developing novel multi-functional materials such as photoferroelectrics.

RESULTS AND DISCUSSION

Symmetry analysis and structural characterizations

$CsGeX_3$ crystalizes in a perovskite structure at room temperature (RT) with a rhombohedral distortion from the pseudo-cubic framework, as illustrated in Fig. 1A (X as Br here). The distortion of the octahedra originates from the Ge displacement from the center of the octahedron, along the direction parallel to the body diagonal of the pseudo-cubic cell ($<111>_{pc}$), which contributes to the electric dipole formation in each unit cell. $CsGeBr_3$ exhibits a low-symmetry rhombohedral phase below 238 °C (511 K) (*25*) and that transforms into a high-symmetry cubic phase at higher temperature (Fig. 1A). The displacement of the Ge ion in the low-symmetry phase along the body diagonal of the pseudo-cubic structure yields three longer Ge-Br bonds (3.051 Å) and three shorter ones (2.541 Å); this structure can also be viewed as an arrangement of tetrahedrally coordinated $[GeBr_3]^-$ units. The stereochemically active lone pair ($4s^2$) of Ge (II) cation can play a central role in promoting the Ge off-centering displacement (*26*) and stabilizing structural distortion that generates the spontaneous polarization.

Through an atmospheric-pressure CVT growth process developed in-house (Materials and Methods), $CsGeBr_3$ (CGB) nanoplates and nanowires were successfully obtained, which were

5

subsequently used as the model systems for structural characterizations and studies of the material properties. The CGB growth via CVT does not require sophisticated conditions and is also compatible with various substrates including silicon, mica, quartz and oxide perovskites. Fig. 1B represents the topographic feature of an assembly of uniformly distributed square CGB nanoplates taken from atomic force microscopic (AFM) imaging, with lateral width of micron scale and thickness on the order of hundred nanometers. We transferred a very thin nanoplate from the growth substrate to the copper grid for transmission electron microscopy (TEM) studies. Energy dispersive X-ray spectroscopic (EDS) measurement and mapping from TEM confirmed the correct atomic ratio as Cs:Ge:Br $\cong$ 1:1:3 for the CGB nanoplate (fig. S2). A selected area electron diffraction (SAED) pattern is also shown in Fig. 1B, together with the corresponding TEM image (inset), indicating the single crystalline nature of the CGB nanoplate and also revealed a pseudo-cubic crystal symmetry. Indexing of this SAED pattern with pseudo-cubic indices in the (001) projection yields the average lattice spacing of 5.635 Å for {100} planes and a distortion angle of 1.3° from the cubic symmetry, in agreement with the standard crystallographic data (*27*). We thus identified that the edges of nanoplate are oriented in the <100> direction while the top surface is the (001) facet. Such symmetry correlations between the crystal structure and the sample geometry can be attributed to the high pseudo-cubic symmetry of the germanium halide perovskites. We also present a typical morphology and crystallographic information of the CVT-grown CGB nanowires with scanning electron microscopic (SEM) image and SAED pattern with the corresponding TEM image (Fig. 1C). Elemental distribution and ratio were also confirmed by EDS mapping on individual nanowires (fig. S3). Controlled growth helped producing CGB nanowires in either horizontal distribution or vertical alignment to the substrates for different characterizations and measurements (fig. S4).

6

Structural analysis for the overall CVT-grown CGB crystals assembly using both synchrotron X-ray microdiffraction (Fig. 1D) and laboratory powder X-ray diffraction (fig. S5) further demonstrated the rhombohedral phase and confirmed the pseudo-cubic lattice parameter of 5.635 Å. Besides the macroscopic structural analysis through XRD, Raman spectroscopy serves as a great tool for observing the vibrational properties of the local symmetry. As shown in Fig. 1e, the Raman spectrum of the CGB nanoplates confirmed this characteristic with the three most representative peaks, 138 cm^{-1}, 163 cm^{-1}, and 210 cm^{-1} corresponding to the E, A_1 (transverse), and A_1 (longitudinal) modes, respectively, of the 3m (C_{3v}) symmetry. Additional Raman peaks in low-frequency (< 100 cm^{-1}) range are shown in fig. S6, all consistent with earlier studies for bulk crystals (*28*). The inversion symmetry breaking in these CGB nanoplates is corroborated by the presence of second harmonic generation (SHG). The optical SHG effect is characterized as exactly doubling the fundamental light frequencies, with the SHG intensity quadratically depending on the input power of fundamental light (fig. S7). Temperature-dependent SHG (fig. S8) exhibits an abrupt change in the SHG intensity of CGB at around 238 ℃ (T_C, Curie temperature), which further verifies the phase transition from a non-centrosymmetric phase at low temperature to a centrosymmetric phase at high temperature.

Semiconductor behaviors

As an illustration of the semiconducting property in this class of perovskite, we first determined the bandgap of the CGB nanoplates from ultraviolet-visible (UV-vis) absorption spectroscopy as around 2.38 eV (fig. S9A), which is narrower than ferroelectric perovskite oxides. The sharp absorption edge also indicates that it is a direct bandgap semiconductor as for the lead halide perovskites. Additionally, UV-vis absorption spectroscopy results from all $CsGeX_3$ (X=Cl, Br, I)

crystals verified their light absorption behavior within the visible spectrum range, with bandgaps of 1.6–3.3 eV (Fig. S9B). We also measured the current-voltage (I-V) characteristics of the CGB nanowires under dark and light conditions (fig. S10). The conductance under light illumination can increase to 5-10 times of that under dark condition, again a characteristic photoresponse for typical semiconductors. As a ferroelectric semiconductor, the resistivity (under dark) of the germanium halide perovskite are around $10^6 - 10^8 \ \Omega \cdot cm$, several orders of magnitude lower than that of the conventional ferroelectric perovskite oxides.

Analysis of ferroelectric polarization

To understand the origin of ferroelectricity in CsGeBr$_3$, we performed *ab initio* calculations to investigate the high- and low-symmetry structures, and the resulting spontaneous polarizations. The details of the calculations and the full set of results for the CsGeX$_3$ series (X = Cl, Br, I) are given in the Methods and Table 1, respectively. Our discussion here is focused on the case of CsGeBr$_3$. Firstly, we performed full structural optimizations of both the high-symmetry cubic $Pm\bar{3}m$ phase and the low-symmetry polar rhombohedral $R3m$ phase, finding that the latter phase is 85 meV/f.u. lower in energy as expected. Next, we calculated the spontaneous polarization (P$_s$) using the Berry phase approach by interpolating between the undistorted (cubic) structure and the polar (rhombohedral) structure to identify the correct branch cuts for polarization values(*29, 30*). Our results are summarized in Fig. 2A with the total polarization calculated being a sum of the ionic and electronic contributions, giving a final value 19.7 µC/cm^2 in the RT distorted phase along the <111> direction. The spontaneous polarization of CsGeBr$_3$ can also be estimated from multiplying the Born effective charges (BECs) of the displaced ions by their displacements in the polar structure (Table 1). For CsGeBr$_3$, we calculate the BEC of Ge to be 5.37*e,* and with a Ge

displacement of 0.27 Å, resulting in a P_s of 12.2 μC/cm^2. This is smaller than the value obtained from the Berry phase approach, indicating a significant electronic charge re-distribution. The anomalously high values of the BEC compared to its formal ionic values of $2e$ in the Ge^{2+} indicates significant charge transfer between cations and anions in this structure, and is a strong indicator of ferroelectric polarization. Finally, we investigate the origins of ferroelectricity in CsGeBr$_3$, which could be potentially driven by the stereochemically active $4s^2$ lone pair on the Ge (II) (*26*). In fig. S11 of Supplementary Materials we plot the real-space charge density for the polar $R3m$ structure, indicating an acentric electronic distribution along the <111> direction, corresponding to the Ge off-centering. We also calculated the orbital-projected density of states (fig. S12) which shows that the top of the valence band comprises mainly of Ge-s and Br-p states, as expected for $4s^2$ lone pair driven ferroelectricity.

The key experimental signatures of the ferroelectric polarization in CsGeBr$_3$ were obtained and are detailed in this and following sections. First, the atomic-resolution scanning transmission electron microscopy (STEM) imaging can be used for characterizing the polarizations and structural distortions from the atomic level. Fig. 2B exhibits a high-angle annular dark field (HAADF) of STEM image taken from a domain (with zone axis of [001]$_{pc}$) on the CGB nanowire, where the atomic-scale polarization mapping was performed using a displacement vector-mapping algorithm (Materials and Methods). This displacement vector map displays atomically resolved lattice distortion and polarization distribution, with the average magnitude of the displacement vector for each atom of ~ 6 pm, consistent with the calculated spontaneous polarization values discussed above. As the CGB nanowires are extremely beam-sensitive at room temperature for STEM imaging (fig. S13), we obtained the useful STEM images on sample at liquid nitrogen

temperature. It should be noted that there is no phase transition in $CsGeBr_3$ at such low temperature (*25*).

To examine the macroscopic polarization and electrical switchability of $CsGeX_3$, we performed the ferroelectric hysteresis measurements. We first fabricated a $CsGeBr_3$ nanowire device and measured the hysteresis loops as shown in fig. S14 and S15. From the polarization-electrical field (P-E) hysteresis loop one can identify an experimental value of Ps in $CsGeBr_3$, to be around 12-15 $\mu C/cm^2$. However, we note that the hysteresis loop does not saturate, i.e., these are minor loops, likely because of the limitations in the maximum applied electric field due to this undesirable device design (see discussions in Supplementary Materials). It could also be due to the effects of leakage current and dielectric contribution convoluting the observed hysteresis loop. Especially, the low resistivity of the $CsGeX_3$ may contribute to a strong leakage current contribution to the unsaturated hysteresis loops. In order to mitigate such effects, we performed pulsed measurements of ferroelectric polarization, known as the Positive-Up-Negative-Down (PUND) test (*31*, *32*). The PUND result (fig. S16) also reveals above-zero switched polarizations (or charges). Furthermore, we developed a more preferrable test protocol based on device with a thin-film geometry as shown in Fig. 2C (see Methods). To reveal the typical P-E loop resulting only from the polarization switching contribution, we measured the current-electric field loop and obtained a reconstructed P-E loop (Fig. 2D) after subtracting the leakage current contribution (see Supplementary Materials, fig. S17 and S18). From this saturated hysteresis loop, we can have more accurate interpretations on the coercive field and remanent polarization of the $CsGeI_3$ film, which are around 40 kV/cm and 20 $\mu C/cm^2$, respectively.

Piezo-response force microscopy and local switching spectroscopy

We further probed the piezoelectric response and ferroelectric domain formation of the CGB nanoplates using piezo-response force microscopy (PFM). The ferroelectric-phase CGB features a spontaneous polarization oriented along one of the eight <111> directions in the pseudo-cubic cell (fig. S19). Since the two-dimensional (2D) geometry of CGB nanoplate is a projection of the 3D nature in crystal lattice, we used vector PFM to completely reveal the polarization orientations and associated domain configuration. With direct correspondence to the crystal symmetry, the CGB nanoplates serve as an ideal platform for investigating how the polarization directions are distributed among different domains. Fig. 3A and 3B present the PFM phase images of one CGB nanoplate under two orthogonal in-plane modes, while the corresponding out-of-plane phase and AFM topographic images are shown in fig. S20. From the in-pane PFM phase images, the in-plane projection of polarization in this individual nanoplate can be interpreted, which contains four vectors pointing outward towards the nanoplate corner, all in parallel to the face diagonal direction. The out-of-plane polarization component is upward (fig. S20A). As a result, the different polarization orientations in the four domain variants can be represented with the four vectors (P_1, P_2, P_3, P_4) shown in Fig. 3C. Each of them corresponds to one of the <111> directions in pseudo-cubic cell. Therefore, it is clear that the CGB nanoplate with thickness of 130 nm (fig. 20C and D) favors to form this divergent domain configuration. These microscopic domains (typically with several microns in width) form due to the net uniformly oriented polarization vector in each of them. A schematic overview of the domain configuration with geometric correspondence to the nanoplate was presented in fig. S20B. Another separate example of domain imaging by in-plane phase contrast is presented and accompanied by the corresponding topographic imaging (Fig. 3D, e). Notably, the CGB nanoplates all display stronger phase contrasts in the in-plane PFM images than in the out-of-plane ones, indicating that the in-plane polarization orientation varies but the

out-of-plane is common on a single CGB nanoplate. Various domain patterns may appear on different nanoplates with different thicknesses, as shown in fig. S21 and S22. We also observed a striped, twin-like domain pattern (along $<110>_{pc}$ direction) on the nanoplate shown in Fig. 3D and 3E, with the magnified in-plane amplitude images in Fig. 3F and corresponded line profile in Fig. 3G. The spacing of the stripes is measured to be around 80 to 100 nm, suggesting the domain width of the nanometer scale, apparently distinctive from that of the microscopic domains. The formation of these twin-like domains (also in fig. S23) can be attributed to the variation of polarization directions in these small domains that would all contribute to the net direction of polarization in a larger microscopic domain, which is a quite common phenomenon in ferroelectric domain structures.

Along with the phase contrast imaging from PFM, local switching spectroscopy was performed to demonstrate the polarization switching behavior under the applied electric field. The piezoelectric behavior in the out-of-plane direction, manifested by the 180° phase hysteresis and the butterfly-shape amplitude loops (Fig. 3H), further supported the ferroelectricity in $CsGeBr_3$. We performed this measurement for the CGB crystals (1μm-thick) grown on a conductive oxide perovskite film, i.e. $SrRuO_3$ (SRO) as a bottom electrode. As a consequence of inverse piezoelectric effect, the amplitude signal can represent the surface displacement of a local point area as a function of electric field applied to the scanning probe tip. The shift and asymmetry of the loop is due to the asymmetrical electrical contacts for top (Pt/Ir-coated Si) and bottom (SRO) electrodes.

Polarization-resolved second harmonic generation imaging

In addition to the scanning probe techniques, the polarization-resolved scanning SHG microscopic imaging, as a fast and non-invasive nonlinear optical method, offers an alternate way to investigate the correlations of structural symmetry, polarization and domain configurations. Fig. 4A depicts the experimental geometry, where the sample orientation can be aligned with the lab coordinate axes and the polarization of fundamental light can be well controlled. The scanning microscopic imaging provides a spatial map of SHG intensity over the sample surface when illuminated with the fundamental beam (Materials and Methods). SHG is known as a domain symmetry-sensitive technique for probing polar material (*33*). While the existence of SHG signal demonstrated the inversion symmetry breaking and spontaneous polar state in the material shown in fig. S7 and S24, the dependence of SHG intensity on the fundamental light polarization can further reveal the local structural symmetry and the correlated spontaneous polarization variance of ferroelectric domains. Fig. 4B shows a polar plot that describes the relationship between the SHG intensity $I_{2\omega}$ and the polarization angle φ for a single spot on a CGB nanoplate, which was obtained from a series of spectra under different φ values in a polarization sweep. It was identified that the SHG intensity varies with φ and reaches the highest and lowest with an interval of 90°. We further acquired the SHG intensity map by scanning over the entire nanoplate at several representative polarization angles, $\varphi = 45°, 90°, 135°, 180°$, as exhibited in Fig. 4C, D, E, F, respectively. It is thus possible to determine the direction vector of the ferroelectric polarization, $\boldsymbol{P}_s$, from the SHG intensity, on the basis of nonlinear optical tensor and conversion equations (fig. S25). However, it is not possible to distinguish between domains with antiparallel polarization, that is, to know the sign of $\boldsymbol{P}_s$. Based on the domain structure we obtained from the PFM phase contrast imaging, we found that the divergent type of domain configuration on the nanoplate still fit for our SHG domain imaging results. It is worthwhile to mention that, for $\varphi = 45°$ and $\varphi = 135°$, the SHG intensity contrast

(bright and dark regions) between domains switches, when the fundamental light polarization is orthogonal to each other (see analysis in Supplementary Materials). This phenomenon also verifies that the in-plane component of spontaneous polarization is parallel to the surface diagonal direction of the nanoplate, which is 45° with respect to the nanoplate edge. Thus, for intermediate states $\varphi = 90°$ and $\varphi = 180°$, there is no observable contrast among the different domains as expected.

In summary, we have presented a comprehensive study on the emergence of ferroelectricity in a semiconducting all-inorganic halide perovskite $CsGeX_3$, based on multi-level understanding and characterization from atomic to mesoscopic and macroscopic scales. The experimental findings in this work may inspire a series of important questions and directions for future exploration. For example, the mechanisms of ferroelectric domain formation could depend on the composition (X=Cl, Br, or I), crystal geometry and sample thickness. Further investigations into the domain microstructures and atomic-scale polarization distributions would also be of great interest regarding this new ferroelectric halide system. Also, different excited-state carrier dynamics or structural phase transitions may occur in a ferroelectric semiconductor upon photo excitation. The coupling between optical functionalities and ferroelectric responses might enable emerging physical phenomena and novel functionalities for material applications, such as light-controlled switches, ferroelectric photovoltaics, piezo-photonics and other photoferroelectrics devices.

MATERIALS AND METHODS

Synthesis of nanostructures. The $CsGeBr_3$ perovskite nanowires and nanoplates were grown by a chemical vapor transport (CVT) method modified from the protocol for $CsPbBr_3$ synthesis that

were previously developed (*34–37*) and were conducted in a tube furnace (Thermolyne 79300). An alumina boat loaded with mixed precursors of CsBr (99.999% trace metal basis, Sigma Aldrich) and $GeBr_2$ (97%, Sigma Aldrich) in a 1:1 molar ratio was put at the heating center of a 1-inch-diameter quartz tube. The substrates used for growth are either the freshly cleaved muscovite mica (Grade V2, Ted pella, Inc.) or Si wafer with amorphous silica on surface, which were placed at a specified position in the downstream region of the tube, which is 17-19 cm away from the tube center. A carrier gas of high purity N_2 (99.999%) or Ar with a flowing rate of 200 sccm was used to purge the whole tube system in order to eliminate oxygen and moisture in the tube before materials growth. In the growth process, the center temperature was set to ramp from room temperature to 400 °C with a heating rate of 50 °C/min and then was maintained at 400 °C for 35 min to achieve the desirable nanoplates growth. The furnace was then shut down and the whole growth system was naturally cooled down to room temperature. During the entire growth process, the gas flow rate was set and stabilized at 100 sccm. After the growth was completed, the samples should be taken out and stored in an Ar-filled glovebox, ready for the following characterizations. Both of nanowires and nanoplates can form on mica and Si substrates. Longer nanowires tend to form on the hotter side (170-180 °C) of the mica, while the majority of nanoplates can be found on the center region (140-160 °C) of the mica. Nanowires and nanoplates grown on Si can be more easily transferred to other substrates (e.g. TEM grid) since most of them are not horizontally distributed but vertically aligned or inclined to Si surface instead. Note: The growth of $CsGeCl_3$ and $CsGeI_3$ nanostructures should also be realized by replacing the Br precursors to Cl or I precursors. Same steps are followed, with slight modifications applied.

X-ray microdiffraction and diffraction. Synchrotron X-ray microdiffraction was performed at Beamline 12.3.2 of the Advanced Light Source, Lawrence Berkeley National Laboratory (LBNL).

The CGB sample was loaded on a stage after sealing with Kapton tape to eliminate air exposure. The stage was rotated and maintained at 20° with respect to the horizontal direction. The detector (DECTRIS Pilatus 1M) was located at 40° with respect to the direct beam and around 151.014 mm from the sample. The detector geometry was calibrated using a finely ground Al_2O_3 reference sample. The measurement was performed in the monochromatic mode at 8 keV (λ = 1.54982 Å) with the X-ray microbeam directed to a designated area of about 200 μm^2 for the measurement. As the size of X-ray microbeam is 1.5 μm, the diffraction was taken by a raster scanning of the beam over the sample area with a step size around 0.5 μm. The time for each measurement is around 20 min, with a data collection of around 100 frames that can be added together and generate the 2D diffraction images. The 2D diffraction images were processed using the X-ray microdiffraction analysis software (XMAS) to obtain the 1D XRD patterns by integration. The other XRD patterns were acquired from a Bruker AXS D8 Advance Diffractometer equipped with a lynxeye detector (Cu Kα radiation, λ = 1.54056 Å).

Scanning electron microscopy (SEM) and Transmission electron microscopy (TEM). SEM images were acquired using a JEOL JSM-6340F field emission scanning electron microscope and a FEI Quanta 3D FEG/FIB SEM (FEG/FIB). For TEM, the CGB nanoplates and nanowires were transferred by lightly pressing a TEM grid on a substrate grown with dense materials. The TEM images and SAED patterns in Fig. 1 and EDS mappings in Fig. S2 and S3 were acquired by FEI Titan microscope at the National Center for Electron Microscopy facility of the Molecular Foundry at LBNL. The electron microscope was operated at 300 kV for all measurements.

Scanning transmission electron microscopy (STEM) and displacement vector mapping. STEM HAADF imaging was carried out on a JEOL Grand ARM300CF equipped with a cold field emission gun and double spherical aberration correctors with a spatial resolution of ~ 0.7 Å

operating at 300 keV in Irvine Materials Research Institute at the University of California, Irvine. STEM images were taken with the convergence angle of the incident electrons at 32 mrad and the collection angle at 90-165 mrad.

The high resolution HAADF STEM imaging provides spatial resolution adequate to measure the atomic positions of the A and B site cations of CGB. The high frequency noise was removed by applying an annular mask in frequency space, and then the initial peak positions were determined by identifying local maxima and refined by fitting Gaussian curves to obtain the atom center positions. Displacements were calculated as the difference between the center of each cation and the center of mass of its for adjacent neighbors.

Cs and Ge atomic positions were measured by using two-dimensional (2D) Gaussian fitting on their atomic columns to locate centers and record offsets. The polarization vectors on Ge is defined as the displacement of Ge atom from the center of unit cell formed by the four Cs and four Br atoms. The polarization vectors on Cs is defined as the opposite displacement of Cs atom from the center of the unit cell formed by the four Ge and four Br atoms.

UV-Vis and Raman spectroscopy. The absorption spectrum was obtained by means of an ultraviolet-visible spectrometer (UV-3101, Shimadzu). The Raman spectroscopy was acquired from a Horiba Jobin-Yvon LabRAM confocal microscope with a 100X (0.60 N.A.) objective. A 633 nm laser (10 mW) was focused on the CGB nanoplates sample and the Raman scattered photons were dispersed by 1800 g/cm grating and collected by the spectrometer, with data collection time of 100 s (exposure time: 10 s and accumulation number: 10). The analysis of Raman spectrum was performed in Igor Pro software with multi-peak fitting function.

Nanowire devices fabrication for electrical measurements. A shadow mask method and a DC/AC sputter system or a thermal evaporator were used to deposit metal contact as electrodes

for the electrical measurements. Commercial TEM grid was employed as a shadow mask (purchased from TED PELLA, Inc. 150 mesh, Model: 12563-CU) and was placed directly on top of substrates grown with $CsGeBr_3$ nanowires. The nanowires with TEM grid masks were subsequently sent into the chamber of a DC/AC sputter system (Edwards 306) for electrode deposition. Cr (which serves as an adhesion layer) and Cu film are deposited by bombarding the target material with high-energy ions from a plasma. The total thickness of the electrode is around 800 nm – 1um.

Thin film device preparation. The $CsGeI_3$ thin films were prepared using thermal evaporations of two separate layers of CsI and GeI_2 sequentially on Pt-deposited SiO_2 substrate, followed by an annealing process to promote the formation of perovskite films (*38*). This film preparation method is not easily transferable to $CsGeBr_3$ so that we performed measurements on the $CsGeI_3$ films as the two share similar ferroelectric properties indicated by the structural origins and theoretical calculations. The Cu electrodes pattern was deposited also by thermal evaporation with the TEM grid (from TED PELLA, Inc. 400 mesh, Model: 12575-CU) as the shadow mask.

Macroscopic polarization-electric field (P-E) measurement. Ferroelectric measurements (P-E loop and PUND test) were taken using a Radiant Technologies Precision Multiferroic tester, and were performed using tungsten (W) probes to contact with the fabricated metallic electrodes. Hysteresis loops were taken at 10-20 kHz.

Current–Voltage (I-V) characteristics measurement. The measurements were conducted on a single nanowire under vacuum in a probe station (Lakeshore CPX-HF) located at the Molecular Foundry of LBNL. The light source used for illumination was a 300 W Xenon lamp (Asahi Spectra MAX-303) equipped with a bandpass filter of 360-580 nm. An Agilent 4155C Semiconductor Parameter Analyzer was used for the electrical measurements.

Piezoresponse force microscopy (PFM) and local switching spectroscopy. PFM measurements were performed using a commercial scanning probe microscope (Asylum MFP-3D). Dual AC resonance tracking (DART) mode of PFM was conducted using a conductive Pt/Ir-coated probe tip (NanoSensor PPP-EFM) to image the domain structures and measure switching-spectroscopy piezoelectric hysteresis loops. The topographic AFM images can be obtained simultaneously from the contact mode of PFM scanning. For the vector PFM containing two in-plane PFM and one out-of-plane PFM imaging, we rotated the sample by 90° between the two in-plane PFM measurements. The local switching spectroscopy was performed using the same setup and probe tip on the CGB crystals grown on SRO film (conductive, as bottom electrode). A triangular voltage waveform (frequency 0.025 Hz, bias of 8 V) was applied to collect both of the amplitude and phase signals of modulated tip vibration as functions of the bias voltage. The driving amplitude of the tip is 1 V.

Second harmonic generation (SHG) measurement and microscopic polarimetry imaging. SHG measurements were performed in the Imaging Facilities of Molecular Foundry at LBNL. The light coming from a Coherent Chameleon Ultra II Ti:Sapphire laser (700-1000 nm) with a pulse width of 150 fs and a repetition rate of 80 MHz was applied for the SHG spectroscopic and microscopic measurement. The incident light (frequency ω) was coupled into the microscope using a dichroic mirror (reflective for light of frequency ω, transparent for frequency 2ω), then was focused onto the sample with a 100X (0.95 NA) Nikon LU Plan Apo objective and scanned across the sample for measuring SHG in a reflection geometry (Fig. 4A). The fundamental beam is exactly parallel to the optical axis of the microscope and incident on the sample at normal incidence. A short-pass filter (580 nm) was employed inside the microscope to block the remaining fundamental beam (900 – 1000 nm) and separate out only the SHG photon (450 – 500 nm). The generated SHG signals were collected on an Andor Kymera Spectrometer and an Andor iXon CCD

19

or an MPD avalanche photodiode (APD) detector for counting photons. The spectrometer can be used to confirm the detected photons at half of the wavelength of fundamental beam. The scanning SHG imaging was obtained through software-controlled moving of the MadCityLabs *xyz*-piezo stage where the sample was loaded. The scanned image has a diffraction-limited lateral resolution of the order of 300-500 nm for a fundamental wave in the near-infrared range.

The wavelength-dependent SHG spectra were acquired at three individual pumping wavelengths at 900 nm, 950 nm, and 1000 nm, respectively. All the other measurements were done with the fundamental wavelength tuned to 900 nm. We also acquired the power-dependent SHG spectra for verifying the SHG process by changing the input power of fundamental light, to check if the SHG intensity has a quadratic dependence on the power. The quadratic power dependence of the SHG intensity on the input power of incident light revealed that the signal detected by APD was only due to two-photon processes as expected. The temperature-dependent SHG measurement was performed on sample placed inside a sealed heating cell (home-built) at a low pressure (~ 1 torr, to prevent sample degradation).

In the SHG polarimetry measurement all linear polarization states of input light are available by rotating a half-wave plate (HWP) in the laser beam path. Before the light passes through HWP, there is also a polarizer to enhance the degree of linear polarization. The HWP was mounted on a motorized rotation stage and controlled by the software, allowing for a continuous and precise rotation of incident polarization $E^{\omega}(\varphi)$ in the *x-y* plane of the lab coordinate system (x, y, z), where φ is the azimuthal angle of the fundamental light polarization. The HWP introduces a 180° between components parallel to the fast axis of the wave plate and perpendicular to the fast axis. This allows arbitrarily rotating a linearly polarized state to any other linear state. For example, if the angle between the fast axis of the HWP and polarized light is θ, then the HWP will rotate the

linear polarization state of the incoming light by 2θ. In our experiments, we acquired a sequence of SHG spectra form polarization sweep and scanning SHG intensity mappings at separate input polarizations.

***Ab initio* Calculation Details.** Our Density Functional Theory (DFT) calculations were performed with the Vienna Ab Initio Simulation Package (VASP) (*39, 40*) with projector augmented waves and the Perdew-Burke-Ernzerhof (PBE) exchange-correlation functional (*41, 42*). We treated Cs (*5s, 5p, 6s*), Ge (*3d, 4s, 4p*), Cl (*3s, 3p*), Cl (*4s, 4p*) and I (*5s, 5p*) electrons as valence. We used a planewave energy cutoff of 800 eV and a Gamma-centered k-point grid of 6×6×6. Structural optimizations of the unit cell shape and size in addition to the internal coordinates were performed until the Hellman-Feynman forces were less than 0.01 eV $Å^{-1}$ with the resulting structural details given in the Table S1. The spontaneous polarization was calculated using the Berry phase approach with interpolated structures between the cubic and polar rhombohedral structure used to obtain consistent branch cuts for the calculated polarizations (*29, 30, 43*).

Theory Results for CsGeCl₃ and CsGeI₃. We also calculated the cubic and rhombohedral structures of $CsGeCl_3$ and $CsGeI_3$, and the resulting spontaneous polarization using both the Berry phase approach and estimates from the Born effective charges (BECs). The results of the polarization calculations for the $CsGeX_3$ series are given in Table 1. From the Berry phase approach we find very similar values of the spontaneous ferroelectric polarization across the series, with more significant contributions to the total value coming from electronic part for Cl, and decreasing down the periodic table. This is a result of the decreasing electronegativity difference as we move down the halide column, resulting in less tendency for electronic driven polarization. This is consistent with estimates of the ionic-driven polarization obtained from the BECs – we find

that the calculated polarization increases we move down the halide column due to both the increased BEC and increases Ge off-centering going from Cl to Br to I.

Author contributions: Y.Z. and P.Y. conceived the idea. Y.Z., R.R. and P.Y. designed the research. Y.Z. led the study, conducted the material synthesis, major characterizations and measurements including PFM and SHG. E.P. and A.F. conducted the P-E measurements. S.M.G. contributed to the theoretical calculations. H.H. conducted the STEM imaging and polarization vector mapping analysis under the supervision of X.P.. C.K.L. helped with device fabrication and electrical measurements. T.L. conducted the TEM electron diffraction and EDS characterizations. J.J. assisted with X-ray microdiffraction experiments. E.S.B. built the SHG microscope and assisted with SHG measurements. A.R. and P.B. assisted with the temperature dependent SHG experiments. All authors contributed to writing or commented on the manuscript.

Competing interests: The authors declare that they have no competing interests.

Data and materials availability: All data needed to evaluate the conclusions in the paper are present in the paper and/or the Supplementary Materials.

Figures and Table
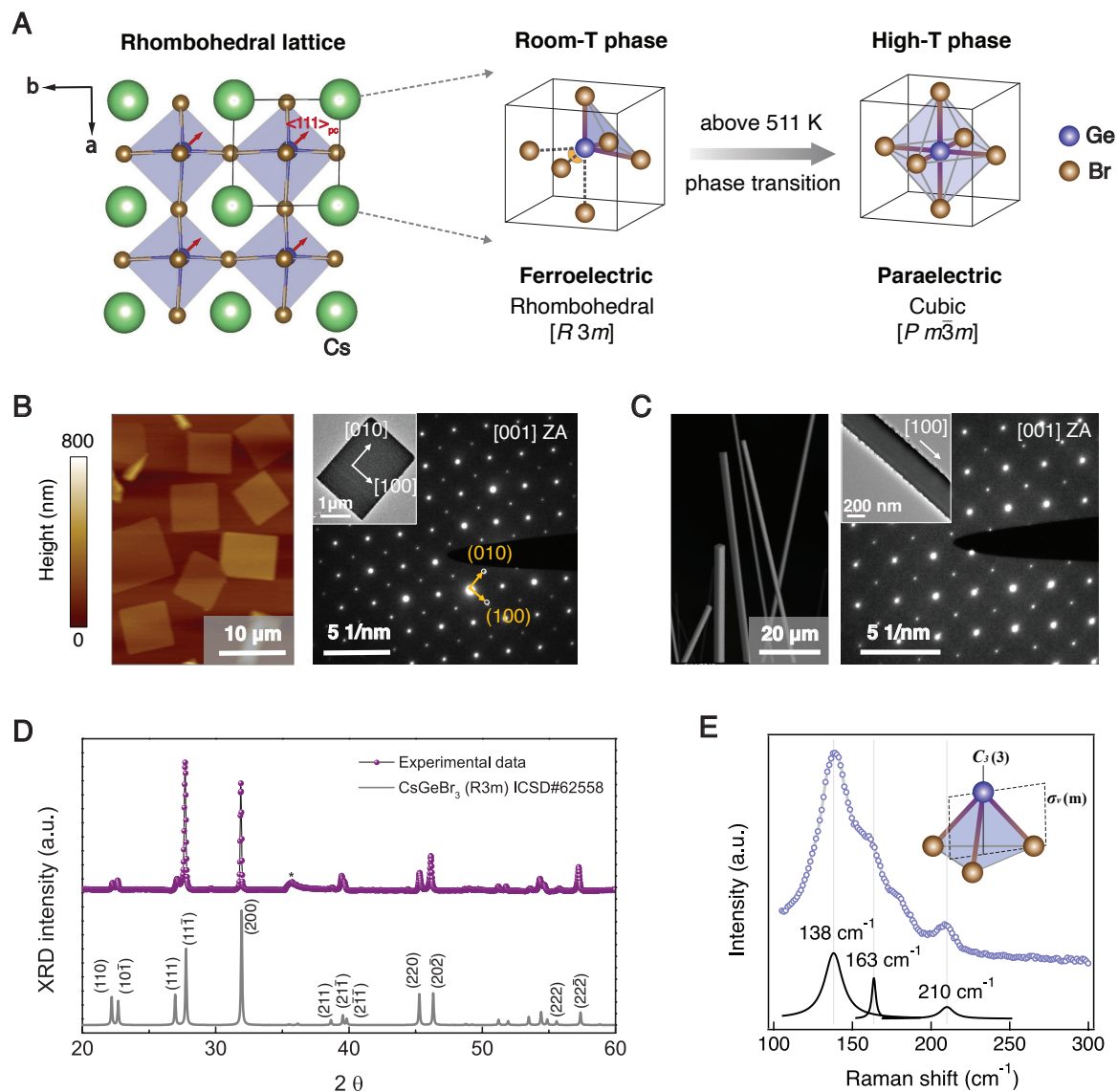
Fig. 1. Structure characterizations of CsGeBr₃ nanostructured single crystals. (**A**) The left panel shows a projected lattice view of CsGeBr₃ (CGB) perovskite structure, which features the Ge displacement along the $<111>_{pc}$ direction in each unit cell. The subscript "pc" denotes pseudo-

cubic. The right panel shows a three-dimensional view of the unit cells to illustrate the Ge coordination environments of CGB in two different phases upon ferroelectric phase transition, where Cs atoms at all corners are not sketched for simplicity. (**B**) A typical topography (AFM) of the CGB nanoplates and the associated SAED pattern from one nanoplate shown in the TEM image (inset) with relevant crystallographic axes and planes labeled. "ZA" denotes the zone axis. (**C**) SEM image of the CGB nanowires and the associated SAED pattern from nanowire shown in the inset TEM image. (**D**) Synchrotron X-ray microdiffraction of an individual CVT-grown CGB crystal at room temperature ($\lambda = 1.54982$ Å). Standard pattern shown in the bottom was indexed using the Inorganic Crystal Structure Database (ICSD). (**E**) Raman spectroscopy of CGB nanoplates at room temperature (633 nm excitation). The phonon modes are related to the $[GeX_3]^-$ tetrahedron with C_{3v} (3*m*) symmetry (inset).
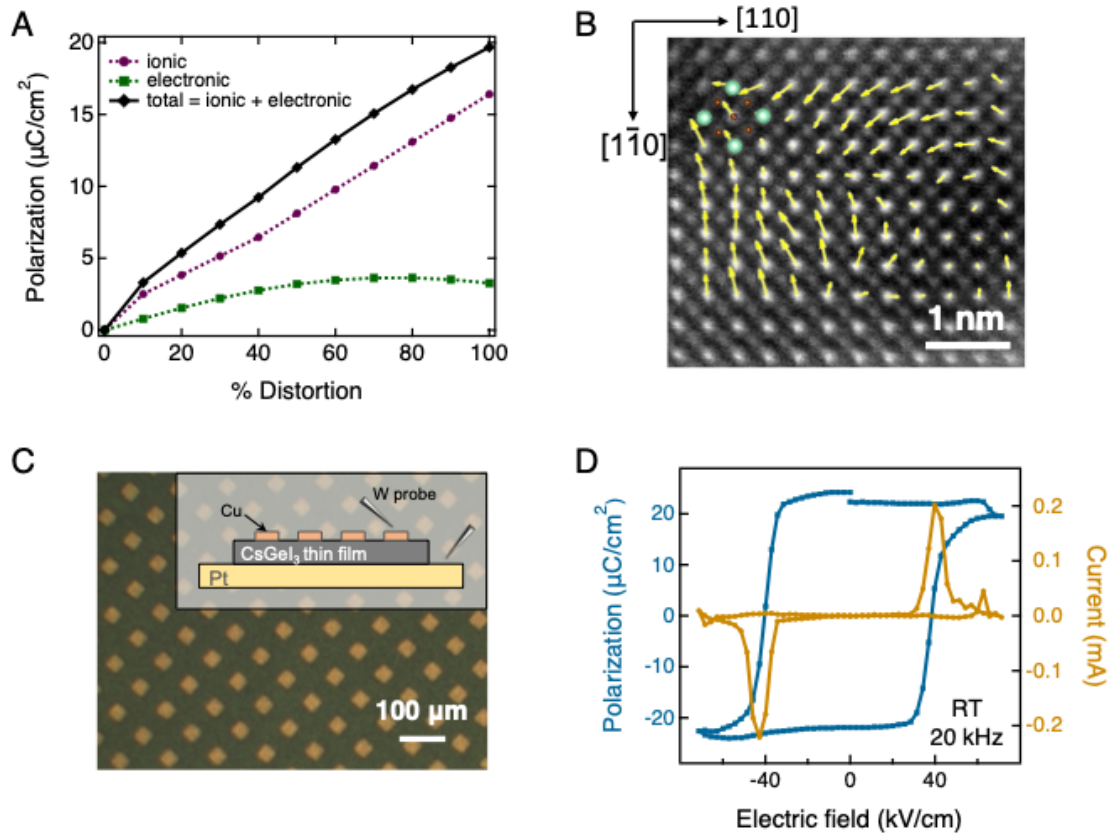
Fig. 2. Theoretical and experimental evidence of the ferroelectric polarizations. (**A**) Berry-phase calculations of the polarization versus distortion percentages for CsGeBr₃, in which 0% distortion means the cubic phase and 100% distortion means the ferroelectric rhombohedral phase. (**B**) Atomic-resolution STEM image on a localized domain of CGB nanowire displays the atomic displacement vector map. (**C**) Optical microscopic imaging of the patterned Cu electrodes (area of each electrode: 30 μm × 30 μm) on the CsGeI₃ thin film (thickness: 350 nm). Inset: Sketched side view of the device structure (Cu-Perovskite film-Pt) for the hysteresis measurement. The voltage is applied to the perovskite film through the two tungsten (W) probes. (**D**) Current versus electric field loop after subtracting the leakage contribution and the corresponding ferroelectric hysteresis loop, obtained from the measurement on the device shown in (C).
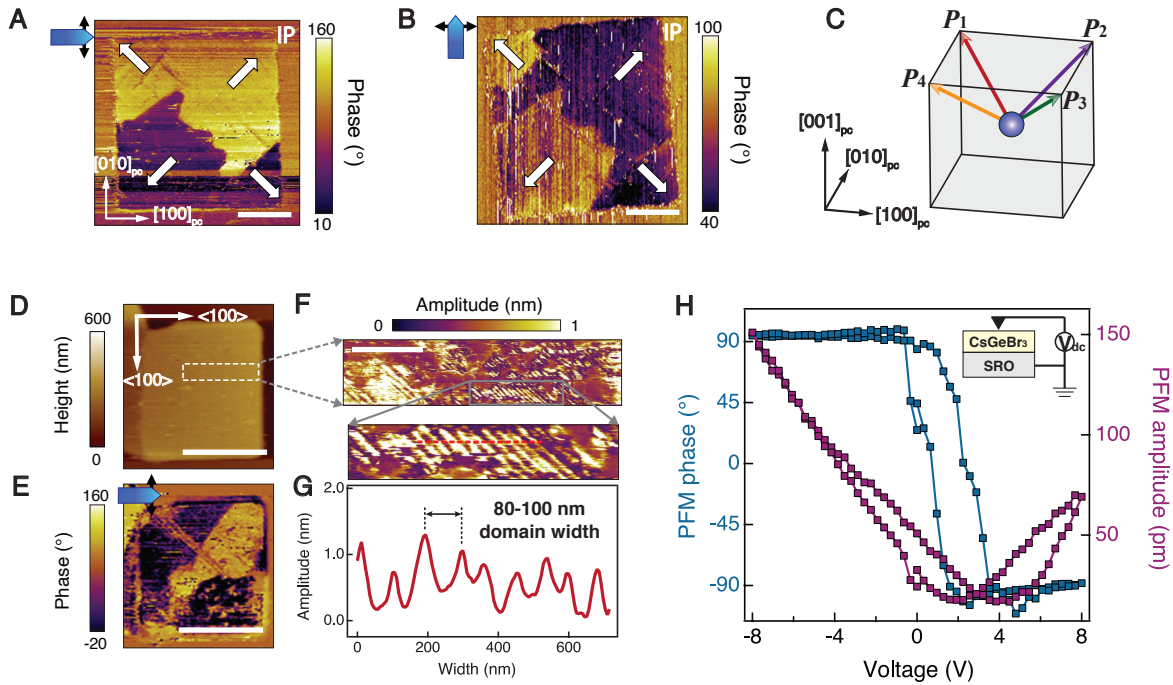
Fig. 3. Piezoelectric response and ferroelectric domain imaging via piezo-response force microscopy (PFM). (**A**) In-plane (IP) PFM phase image of a CGB nanoplate. Scale bar: 5 μm. (**B**) In-plane PFM phase image of the same plate with sample rotation by 90° relative to (A). Scale bar: 5 μm. In both (A) and (B), the blue arrows refer to the cantilevers and the double-ended black arrows correspond to the in-plane polarization components that are detected, perpendicular to the cantilever axis. In-plane projections of the polarizations were shown by the white arrows. (**C**) Polarization vectors in the four domain variants were represented by P_1, P_2, P_3 and P_4 along $[\bar{1}11]$, $[111]$, $[\bar{1}\bar{1}1]$ and $[1\bar{1}1]$ pseudo-cubic (pc) directions, respectively. (**D**), (**E**) AFM image (D) and in-plane PFM phase image (E) of another CGB nanoplate. Scale bars: 5 μm. (**F**) Zoomed-in in-plane PFM amplitude image of a region on the plate indicated in (D). Scale bar: 1 μm. The bottom

shows a further zoomed-in image. (**G**) Corresponding line trace at red dashed line in (F). (**H**) Phase

and amplitude switching spectroscopy loops for the CGB grown on SrRuO$_3$ (SRO) film, which

formed a simple device structure (inset) with DC electric field applied.
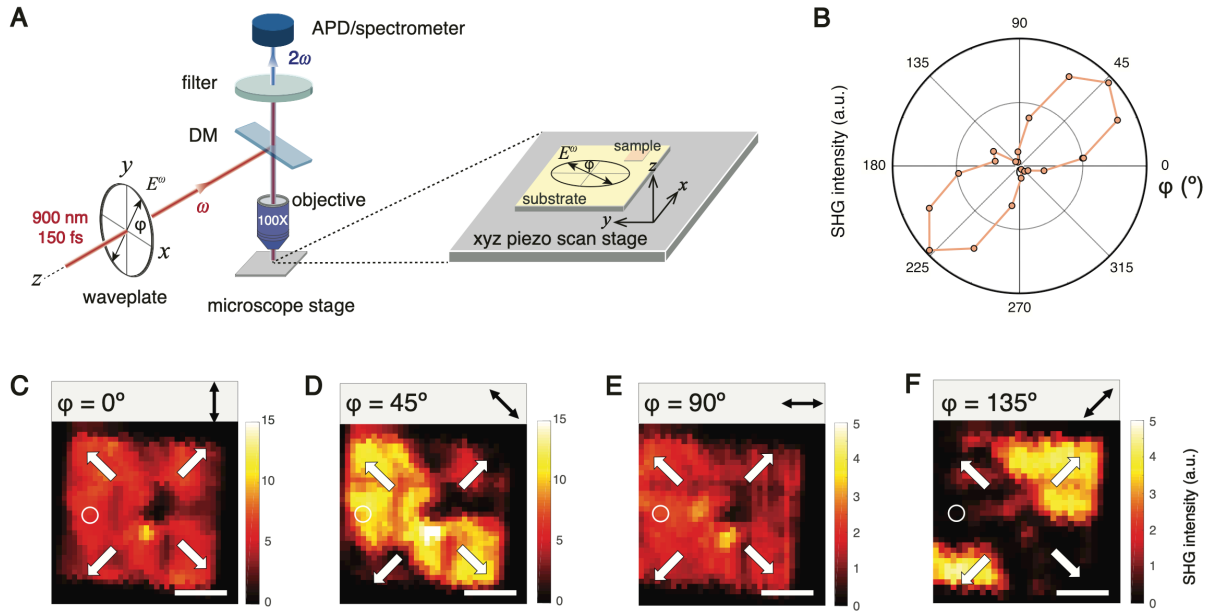
Fig. 4. Light polarization-resolved second harmonic generation (SHG) measurement and spatial mapping. (**A**) Schematic representation of the experimental setup to illustrate the sample orientation with respect to the stage geometry and light propagation direction. The fundamental light pulses (900-nm wavelength) impinge on the sample CGB {001} surface at normal incidence, with a half-waveplate controlling their polarization. SHG light (450 nm) was detected in the reflection-mode scanning microscopy. The fundamental beam propagates along *z* axis in lab coordinate system and polarizes along any direction in the *x-y* plane, where the polarization angle (φ) is defined by the azimuthal angle of incident electric field direction with respect to the *x* axis. DM: dichroic mirror. Filter: 580 nm short-wavelength-pass filter. (**B**) Polar plots of SHG intensity

versus polarization angle (φ) for a region depicted as the white circle on the plate mapped in (c-f). (**C**), (**D**), (**E**), (**F**) Spatial mapping SHG intensity of the domain variants on the CGB nanoplate at different linear polarization states with φ and the double-ended black arrows indicated in each image. The white arrows indicate the possible configuration for the in-plane polarization orientations in the four domains. Scale bars: 5 μm.

Table 1. DFT calculated spontaneous polarization for $CsGeX_3$ (X= Cl, Br, I) for the rhombohedral (*R3m*) phase using both a Born effective charge (BEC) estimation and a full Berry phase calculation, in comparison with the experimental result for $CsGeBr_3$ single crystal and $CsGeI_3$ thin film reported here.

	Born Effective Charge (BEC) (*e*)	**Ge displacement along <111> (Å)**	**P_S (μC/cm^2)** *BEC estimated*	**P_S (μC/cm^2)** *Berry phase calculated*	**P_S (μC/cm^2)** **Experiment**
CsGeCl$_3$	4.799	0.237	10.7	18.5	\
CsGeBr$_3$	5.372	0.271	12.2	19.7	12-15
CsGeI$_3$	6.175	0.318	13.7	18.6	~ 20

References

1. M. E. Lines, A. M. Glass, *Principles and applications of ferroelectrics and related materials* (Oxford university press, 2001).

2. J. F. Scott, Applications of modern ferroelectrics. *Science (80-.).* **315** (2007), pp. 954–959.

3. L. W. Martin, A. M. Rappe, Thin-film ferroelectric materials and their applications. *Nat. Rev. Mater.* **2** (2016), , doi:10.1038/natrevmats.2016.87.

4. V. M. Fridkin, *Photoferroelectrics* (Springer Science & Business Media, 2012), vol. 9.

5. S. Y. Yang *et al.*, Above-bandgap voltages from ferroelectric photovoltaic devices. *Nat. Nanotechnol.* **5**, 143–147 (2010).

6. J. Kreisel, M. Alexe, P. A. Thomas, A photoferroelectric material is more than the sum of its parts. *Nat. Mater.* **11** (2012), p. 260.

7. H. Huang, Solar energy: Ferroelectric photovoltaics. *Nat. Photonics*. **4**, 134–135 (2010).

8. T. Li *et al.*, Optical control of polarization in ferroelectric heterostructures. *Nat. Commun.* **9**, 3344 (2018).

9. T. Choi, S. Lee, Y. J. Choi, V. Kiryukhin, S. W. Cheong, Switchable ferroelectric diode and photovoltaic effect in BiFeO3. *Science (80-.).* **324**, 63–66 (2009).

10. I. Grinberg *et al.*, Perovskite oxides for visible-light-absorbing ferroelectric and photovoltaic materials. *Nature*. **503**, 509–512 (2013).

11. G. Y. Gou, J. W. Bennett, H. Takenaka, A. M. Rappe, Post density functional theoretical studies of highly polar semiconductive Pb(Ti1-xNix)O3-x solid solutions: Effects of cation arrangement on band gap. *Phys. Rev. B - Condens. Matter Mater. Phys.* **83** (2011), doi:10.1103/PhysRevB.83.205115.

12. E. Fatuzzo *et al.*, Ferroelectricity in SbSI. *Phys. Rev.* **127**, 2036–2037 (1962).

13. A. V. Kolobov *et al.*, Ferroelectric switching in epitaxial GeTe films. *APL Mater.* **2** (2014), doi:10.1063/1.4881735.

14. M. M. Lee, J. Teuscher, T. Miyasaka, T. N. Murakami, H. J. Snaith, Efficient hybrid solar cells based on meso-superstructured organometal halide perovskites. *Science (80-.).* **338**, 643–647 (2012).

15. H. J. Snaith, Perovskites: The emergence of a new era for low-cost, high-efficiency solar cells. *J. Phys. Chem. Lett.* **4** (2013), pp. 3623–3630.

16. M. V. Kovalenko, L. Protesescu, M. I. Bodnarchuk, Properties and potential optoelectronic applications of lead halide perovskite nanocrystals. *Science (80-.).* **358** (2017), pp. 745–750.

17. M. A. Green *et al.*, Solar cell efficiency tables (version 51). *Prog. Photovoltaics Res. Appl.* **26**, 3–12 (2018).

18. L. Li *et al.*, A Potential Sn-Based Hybrid Perovskite Ferroelectric Semiconductor. *J. Am.*

Chem. Soc. **142**, 1159–1163 (2020).

19.   Y. M. You *et al.*, An organic-inorganic perovskite ferroelectric with large piezoelectric response. *Science (80-.).* **357**, 306–309 (2017).

20.   Y. Liu *et al.*, Chemical nature of ferroelastic twin domains in CH 3 NH 3 PbI 3 perovskite. *Nat. Mater.* **17**, 1013–1019 (2018).

21.   A. Gómez, Q. Wang, A. R. Goñi, M. Campoy-Quiles, A. Abate, Ferroelectricity-free lead halide perovskites. *Energy Environ. Sci.* **12**, 2537–2547 (2019).

22.   J. A. Steele *et al.*, Phase Transitions and Anion Exchange in All-Inorganic Halide Perovskites. *Accounts Mater. Res.* **1**, 3–15 (2020).

23.   Z. G. Lin, L. C. Tang, C. P. Chou, Characterization and properties of novel infrared nonlinear optical crystal CsGe(BrxCl1-x)3. *Inorg. Chem.* **47**, 2362–2367 (2008).

24.   A. Christensen, S. Rasmussen, A ferroelectric chloride of perovskite type. *Acta Chem. Scand.* **19**, 421–428 (1965).

25.   G. Thiele, H. W. Rotter, K. D. Schmidt, Kristallstrukturen und Phasentransformationen von Caesiumtrihalogenogermanaten(II) CsGeX3 (X = Cl, Br, I). *ZAAC - J. Inorg. Gen. Chem.* **545**, 148–156 (1987).

26.   D. H. Fabini, R. Seshadri, M. G. Kanatzidis, The underappreciated lone pair in halide perovskites underpins their unusual properties. *MRS Bull.* **45**, 467–477 (2020).

27.   U. Schwarz *et al.*, Pressure-induced phase transition in CsGeBr3 studied by X-ray diffraction and raman spectroscopy. *J. Solid State Chem.* **118**, 20–27 (1995).

28.   L. Y. Huang, W. R. L. Lambrecht, Vibrational spectra and nonlinear optical coefficients of rhombohedral CsGeX3 halide compounds with X= I, Br, Cl. *Phys. Rev. B.* **94** (2016), doi:10.1103/PhysRevB.94.115202.

29.   R. D. King-Smith, D. Vanderbilt, Theory of polarization of crystalline solids. *Phys. Rev. B.* **47**, 1651–1654 (1993).

30.   N. A. Spaldin, A beginners guide to the modern theory of polarization. *J. Solid State Chem.* **195**, 2–10 (2012).

31.   A. Grigoriev, M. M. Azad, J. McCampbell, Ultrafast electrical measurements of polarization dynamics in ferroelectric thin-film capacitors. *Rev. Sci. Instrum.* **82** (2011), doi:10.1063/1.3665209.

32.   E. Parsonnet *et al.*, Toward Intrinsic Ferroelectric Switching in Multiferroic BiFeO3. *Phys. Rev. Lett.* **125** (2020), doi:10.1103/PhysRevLett.125.067601.

33.   S. A. Denev, T. T. A. Lummen, E. Barnes, A. Kumar, V. Gopalan, Probing ferroelectrics using optical second harmonic generation. *J. Am. Ceram. Soc.* **94**, 2699–2727 (2011).

34.   D. Lu *et al.*, Giant Light-Emission Enhancement in Lead Halide Perovskites by Surface Oxygen Passivation. *Nano Lett.* **18**, 6967–6973 (2018).

35.   Y. Zhang *et al.*, Quantitative imaging of anion exchange kinetics in halide perovskites. *Proc. Natl. Acad. Sci. U. S. A.* **116**, 12648–12653 (2019).

36.   Y. Wang *et al.*, Photon Transport in One-Dimensional Incommensurately Epitaxial

CsPbX3 Arrays. *Nano Lett.* **16**, 7974–7981 (2016).

37. J. Chen *et al.*, Single-Crystal Thin Films of Cesium Lead Bromide Perovskite Epitaxially Grown on Metal Oxide Perovskite (SrTiO3). *J. Am. Chem. Soc.* **139**, 13525–13532 (2017).

38. K. A. Montiel *et al.*, in *2019 IEEE 46th Photovoltaic Specialists Conference (PVSC)* (IEEE, 2019), pp. 1183–1186.

39. G. Kresse, J. Furthmüller, Efficiency of ab-initio total energy calculations for metals and semiconductors using a plane-wave basis set. *Comput. Mater. Sci.* **6**, 15–50 (1996).

40. G. Kresse, J. Furthmüller, Efficient iterative schemes for ab initio total-energy calculations using a plane-wave basis set. *Phys. Rev. B - Condens. Matter Mater. Phys.* **54**, 11169–11186 (1996).

41. P. E. Blöchl, Projector augmented-wave method. *Phys. Rev. B.* **50**, 17953–17979 (1994).

42. J. P. Perdew, K. Burke, M. Ernzerhof, Generalized gradient approximation made simple. *Phys. Rev. Lett.* **77**, 3865–3868 (1996).

43. R. Resta, Macroscopic polarization in crystalline dielectrics: The geometric phase approach. *Rev. Mod. Phys.* **66**, 899–915 (1994).

44. V. M. Goldschmidt, Die Gesetze der Krystallochemie. *Naturwissenschaften.* **14**, 477–485 (1926).

45. C. J. Bartel *et al.*, New tolerance factor to predict the stability of perovskite oxides and halides. *Sci. Adv.* **5** (2019), doi:10.1126/sciadv.aav0693.

46. L. C. Tang, J. Y. Huang, C. S. Chang, M. H. Lee, L. Q. Liu, New infrared nonlinear optical crystal CsGeBr3: Synthesis, structure and powder second-harmonic generation properties. *J. Phys. Condens. Matter.* **17**, 7275–7286 (2005).

47. H. Yan *et al.*, The contribution of electrical conductivity, dielectric permittivity and domain switching in ferroelectric hysteresis loops. *Prog. Adv. Dielectr.* **1**, 1–20 (2020).

48. J. T. Evans, Characterizing Ferroelectric Materials. *Radiant Technol. Inc*, 1–123 (2011).

49. R. Nechache *et al.*, Epitaxial thin films of the multiferroic double perovskite Bi 2FeCrO6 grown on (100)-oriented SrTiO3 substrates: Growth, characterization, and optimization. *J. Appl. Phys.* **105**, 61621 (2009).

50. L. Corbellini *et al.*, Hysteresis loops revisited: An efficient method to analyze ferroic materials. *J. Appl. Phys.* **120**, 124101 (2016).

51. R. Meyer, R. Waser, K. Prume, T. Schmitz, S. Tiedke, Dynamic leakage current compensation in ferroelectric thin-film capacitor structures. *Appl. Phys. Lett.* **86**, 1–3 (2005).

52. R. W. Boyd, *Nonlinear Optics* (2008).